Carbon 176 (2021) 446–457

Contents lists available at ScienceDirect

Carbon

journal homepage: www.elsevier.com/locate/carbon

Effects of coating layers on the thermal transport in carbon nanotubes-based van der Waals heterostructures

Penghua Ying, Jin Zhang*, Yao Du, Zheng Zhong**

School of Science, Harbin Institute of Technology, Shenzhen, 518055, PR China

ARTICLE INFO

Article history:
Received 26 October 2020
Received in revised form
31 December 2020
Accepted 28 January 2021
Available online 3 February 2021

Keywords:
Carbon nanotube
Boron nitride nanotube
Molybdenum disulfide nanotube
Onedimensional
van der waals heterostructure
Thermal transport
Non-equilibrium
Molecular dynamics simulation

ABSTRACT

In this paper, we conduct a comprehensive investigation on the thermal transport in one-dimensional (1D) van der Waals (vdW) heterostructures by using non-equilibrium molecular dynamics simulations. As for the considered 1D vdW heterostructures having a base of (40,40) carbon nanotube (CNT), we find that the boron nitride nanotube (BNNT) coating can increase the thermal conductance of inner CNT base by 36%, while the molybdenum disulfide nanotube (MSNT) coating can reduce the thermal conductance by 47%. The different effects of nanotube coatings on the thermal transport behaviors of 1D vdW heterostructures are explained by the competition mechanism between the improved heat flux and the increased temperature gradient in 1D vdW heterostructures. The thermal transport in 1D vdW heterostructures containing three layers is also investigated. It is found that the coaxial BNNT-MSNT coating can significantly reduce the thermal conductance of inner CNT base by 61%, which is even larger than the influence of an individual MSNT coating. This work not only provides molecular insights into the heat transport behaviors of 1D vdW heterostructures but also provides guidance for the design of 1D vdW heterostructures with desired thermal properties.

1. Introduction

The two-dimensional (2D) heterostructures have attracted much attention recently under merging different 2D crystals to enable novel physical properties and functional applications [1], such as band-structure engineering [2], ultrafast charger transfer [3], and vertical field-effect transistor [4]. According to the direction of combination, 2D heterostructures can be divided into van der Waals (vdW) heterostructures and in-plane heterostructures. The vdW heterostructures are synthesized by stacking different 2D crystals with weak vdW interactions in the out-of-plane direction. As for their in-plane counterparts, different coplanar 2D crystals are linked via covalent bonds. The development of 2D vdW heterostructures has greatly expanded the 2D material family. Inspired by the fact that a single-walled carbon nanotube (CNT) can be treated as a seamless cylinder rolled from graphene, it is thus expected that the one-dimensional (1D) tubular vdW heterostructures could be obtained by rolling up corresponding 2D vdW heterostructures. However, compared with planar 2D sheets, 1D nanotubes are much more difficult to be synthesized in experiments, since their structures are topologically protected from being stack-nested [5]. Hence, many efforts have been devoted to synthesize 1D vdW heterostructures. Very recently, Xiang et al. [6] made a significant progress in this area. They demonstrated the experimental discovery and controlled fabrication of 1D tubular vdW heterostructures with single crystals, which consist of three different shell components: an inner CNT layer, a middle hexagonal boron nitride nanotube (BNNT) layer, and an outer molybdenum disulfide nanotube (MSNT) layer. In addition to this triple-walled CNT@BNNT@MSNT heterostructure, double-walled 1D vdW heterostructures such as CNT@BNNT and CNT@MSNT were also obtained in their experiment. These obtained 1D vdW heterostructures were found to exhibit numerous unique optoelectronic properties [7].

Due to their superior thermal conductivity and outstanding mechanical stability, 1D vdW heterostructures can serve as promising thermal interface materials in solving the problem of heat dissipation in modern electronic devices [8]. However, the thermal property of 1D heterostructures is still almost unexplored despite that the thermal transport behaviors of their pristine counterparts such as CNT [9,10], BNNT [11], and MSNT [12,13], have been well

* Corresponding author.
** Corresponding author.
E-mail addresses: jinzhang@hit.edu.cn (J. Zhang), zhongzheng@hit.edu.cn (Z. Zhong).

https://doi.org/10.1016/j.carbon.2021.01.146
0008-6223/

investigated. To our best knowledge, among different 1D vdW heterostructures, only the thermal conductivity of CNT@BNNT has been investigated recently based on experimental measurements [14,15] and molecular dynamics (MD) simulations [14]. These studies reported a large enhancement in the thermal conductivity of coaxial CNT@BNNT heterostructures when compared to the isolated CNT. The thermal transport property of other 1D vdW heterostructures such as CNT@MSNT and CNT@BNNT@MSNT that have been successfully synthesized very recently [6], however, remains unknown. Moreover, there are no reports on the interfacial thermal conductance of 1D vdW heterostructures, which is, however, crucial for their applications as nanoelectronics devices [16], since the heat can not only transport along axial direction, but also can conduct through the interface of nanotubes.

Motivated by the above ideas, the thermal conductivity of 1D vdW heterostructures containing two layers (CNT@BNNT and CNT@MSNT) and their counterparts containing three layers (CNT@BNNT@MSNT) is investigated by the non-equilibrium molecular dynamics (NEMD) method. The double-walled CNT, i.e., CNT@CNT, is also considered here for the sake of comparison. It is found that both CNT and BNNT coatings can increase the thermal transport in CNT base, while MSNT and BNNT-MSNT coatings exhibit the opposite effect. The heat flux, temperature distribution together with the vibrational density of states (VDOS) are carefully examined to explain different enhancement/hindering effects of different nanotube coatings on the thermal transport in 1D vdW heterostructures. Besides, the interfacial thermal conductance between the inner and outer nanotubes in 1D vdW heterostructures is also calculated to provide a quantitative understanding of the thermal transport behaviors of 1D vdW heterostructures.

2. Models and methods

2.1. Models

As plotted in Fig. 1, CNT, BNNT, and MSNT are considered in our study. In terms of the number of layers, single-walled, double-walled, and triple-walled nanotubes are considered. Specifically, a CNT (BNNT or MSNT) with the lattice vector of $\boldsymbol{r} = m\boldsymbol{a_1}+n\boldsymbol{a_2}$ ($\boldsymbol{a}_1 = \boldsymbol{a}_2$ are lattice constants of the primitive cell) can be noted as (m, n) CNT (BNNT or MSNT). In the present study, three CNT bases including (40,40) CNT, (70,0) CNT, (20,20) CNT and (60,30) CNT are considered to discuss the influence of chirality and radius on the thermal transport in CNT-based vdW heterostructures. The coating nanotube layers have the same chirality as the CNT base. For example, (40,40) CNT base is coated by (45,45) CNT, (45,45) BNNT and (38,38) MSNT as shown in Fig. 1(a). In other words, double-walled nanotubes including (40,40) CNT@(45,45) CNT, (40,40) CNT@(45,45) BNNT and (40,40) CNT@(38,38) MSNT, and the triple-walled nanotube (40,40) CNT@(45,45) BNNT@(42,42) MSNT as shown in Fig. 1(c) are considered in the present study. For convenience, these nanotube structures are referred to as CNT@CNT, CNT@BNNT, CNT@MSNT, and CNT@BNNT@MSNT, respectively, in the following discussion. The specific atomic structures of the (40,40) CNT based coaxial heterostructures are plotted in Fig. 1(a)–(c).

To simplify the modeling of the coaxial CNT@BNNT structures, the bond lengths of CNT and BNNT are both set as 1.43 Å, which is an intermediate value between the intrinsic values 1.42 Å and 1.45 Å for CNT and BNNT, respectively. Although this treatment can cause the axial lattice mismatch in our initial model of heterostructures, as shown in Figure S1, this axial lattice mismatch is very small, which is 0.24% for CNT layer and 0.41% for BNNT layer at the equilibrium stage, respectively. Meanwhile, at the equilibrium stage the interlayer spacing between CNT and BNNT layers of the CNT@BNNT built here is 3.47 Å, which is very close to the theoretically predicted value of 3.40 Å [17,18]. According to the previous studies on the thermal properties of graphene/h-BN heterostructures [19,20], these small lattice mismatch strains in CNT and BNNT layers have a trivial effect on their thermal conductivity, which thus can be safely ignored. The bond length of MSNT, i.e., the distance between adjacent Mo and S atoms are set as 2.42 Å. Thus, when 4 MSNT unit cells are on top of 5 CNT unit cells as shown in Fig. 1(d), CNT and MSNT can be perfectly matched as a CNT@MSNT supercell (see Figure S2), which is similar to the structure of the supercell of graphene/MoS_2 heterostructures [21,22]. The initial inter-wall distance between the inner CNT layer and the outer CNT layer (or BNNT layer) is set as 3.4 Å, while the inter-wall distance between the CNT layer (or BNNT layer) layer and the adjacent MSNT layer is set as 3.6 Å. These values of inter-wall distance are very close to the results of 2D heterostructures predicted from previous first-principle calculations [23–25]. The OVITO [26] software is employed to visualize the system.

2.2. Molecular dynamics simulations

The molecular dynamics simulation conducted in the present study is implemented by using the publicly available simulation code LAMMPS [27] which has the correct implementation of heat flux for many-body potentials [28], and the standard Newton equations of motion are integrated in time by using the velocity Verlet algorithm. The time step is set as 1.0 fs. All initial structures are first adopted to perform energy minimization. Then, the structures are further relaxed at 300K and 0 GPa along the axial direction for 100 ps using the Langevin thermostat [29] to obtain the equilibrium state. The interactions among C, B, and N atoms are described by the Tersoff potential [30,31], while the interaction between Mo and S atoms in MSNT is described by the REBO potential [32,33], since the previous study [34] suggested that the REBO potential can give a more accurate prediction of thermal transport properties compared to other classical force fields such as the Stillinger-Weber potential [35,36].

The weak vdW interactions between adjacent nanotubes are modeled by 12–6 Lennard-Jones (LJ) potential with the form $V(r_{ij}) = 4\varepsilon[(\delta/r_{ij})$ [12]-(δ/r_{ij}) [6]], where ε, δ, and r_{ij}, respectively, are depth of the potential well, the finite distance at which the interparticle potential is zero, and the distance between atoms i and j. The specific values of parameters ε and θ are set to be $\varepsilon = 2.620$ meV and $\delta = 0.3440$ nm between C atoms, $\varepsilon = 4.116$ meV and $\delta = 0.3453$ nm between B atoms, $\varepsilon = 0.586$ meV and $\delta = 0.4200$ nm between Mo atoms, and $\varepsilon = 13.860$ meV and $\delta = 0.3130$ nm between S atoms [32,37–39]. The arithmetic mix rule is employed to model the LJ potential between different elements. Meanwhile, the cutoff in all LJ potentials is set as 1.0 nm. The corresponding binding energy of one CNT@MSNT heterostructure supercell as plotted in Fig. 1(d) extracted from the LJ potential is −20.4 meV, which is in good agreement with the result around −21.0 meV of graphene/MoS_2 heterostructures previously obtained from first-principle calculations [40].

2.3. Calculations of thermal conductivity

The classical NEMD method was employed in the calculations of thermal conductivity. Specifically, the thermal conductivity k of the investigated nanotubes was extracted with the aid of the following Fourier's law of heat conduction:

$$k = -\frac{J}{A\nabla T} \tag{1}$$

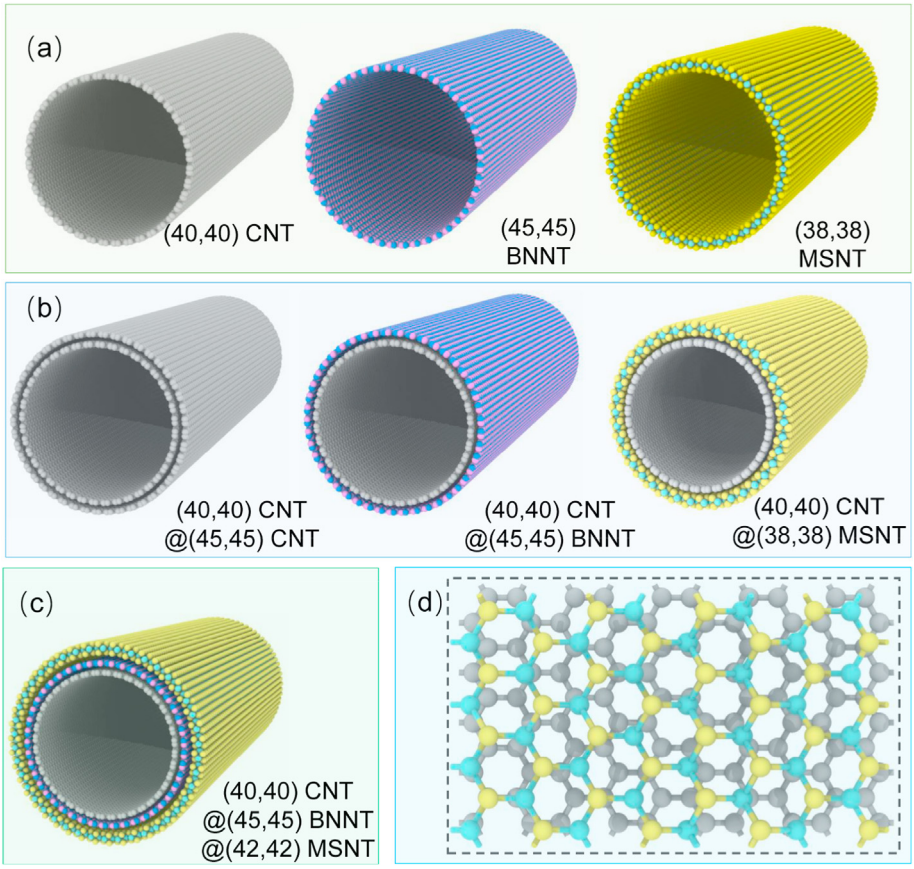

Fig. 1. Atomic representation of different nanotube structures considered here. (a) Single-walled nanotubes (from left to right): CNT, BNNT, and MSNT. (b) Double-walled nanotubes (from left to right): CNT@CNT, CNT@BNNT, and CNT@MSNT. (c) Triple-walled nanotube: CNT@BNNT@MSNT. (d) One supercell of the CNT@MSNT heterostructure with the lattice constant of MSNT and CNT along the axial direction being 3.096 Å and 2.477 Å, respectively. (A colour version of this figure can be viewed online.)

Here J denotes the heat flux along the axial direction of nanotubes.$\nabla T = dT/dx$ is the temperature gradient along the axial direction with T and x being the temperature and the axial coordinate, respectively. A is the cross-sectional area of the nanotube, which can be approximated as $A = \pi[(R_{out}\text{-}r_{out})\ [2]\text{-}(R_{in}\text{-}r_{in})\ [2]]$. Here, R_{in} and R_{out} are, respectively, the radii of inner and outer nanotubes, while r_{in} and r_{out} are, respectively, the thicknesses of inner and outer nanotubes, which are assumed to equal to their vdW diameters. In this study, the thicknesses of CNT, BNNT, and MSNT were assumed to be 0.340 nm, 0.340 nm, and 0.672 nm, respectively, which are the same as the values of their 2D material counterparts [22].

In the above discussion, the thickness of single-walled nanotubes is assumed to equal to the vdW diameter, but many other values also have been proposed for the equivalent thickness of single-walled nanotubes [47–49]. Thus, to surmount the hurdle in identifying the equivalent thickness of the nanotube structures with only one atom or several atoms thickness, we also calculate the quantity of "thermal conductance" $\sigma = kA$. Here, the thermal conductance is defined as the product of the thermal conductivity and cross-sectional area [9], which is different from its conventional definition equaling the thermal conductivity divided by nanotube length [41]. Actually, a similar definition of thermal conductance has been widely employed in the previous studies on the thermal transport properties of various 2D materials and nanotube materials to avoid the uncertainty caused by the arbitrary definition of their cross-sectional areas [9,14,22,42].

As shown in Fig. 2(a), to perform NEMD simulations, the whole nanotube was divided into five regions along the axial direction, which include two fixed regions at the two ends, the adjacent cold and hot regions (i.e., heat sink and heat source), and the middle heat flux region. Two fixed regions were both set as 5 Å in length, while the cold and hot regions were set to have the same length of 10 Å. The temperatures of the cold and hot regions were set as 275 K and 325 K, respectively. The whole simulation box was divided into 40 slabs along the axial direction to record the time-average temperature of each slab for generating the temperature gradient. The heat transport simulation was performed for 1500 ps. Specifically, the stable temperature distribution was achieved within the first 500 ps, while the temperature gradient was obtained by averaging over the last 1000 ps MD simulations, which is graphically shown in Fig. 2(b) for CNT@MSNT with a length of 20 nm. Meanwhile, as shown in Fig. 2(c), the corresponding heat flux J was recorded by averaging the input power of the cold region and the output power of the hot region through $J = (Q_h + Q_c)/2\Delta t$, where Q_c and Q_h are, respectively, the accumulated energies in cold and hot regions (i.e., heat sink and heat source regions) during the running time Δt.

It is noted that only the phonons transport was considered in NEMD simulations, while the contribution of electrons was neglected. This treatment is appropriate for the present 1D vdW heterostructures due to the following reasons. First, BNNT and MSNT components in the present 1D vdW heterostructures are both semiconducting materials [43,44], whose heat carriers are majorly the lattice vibrations or phonons [45,46]. Under this circumstance, the contribution of electrons to their thermal

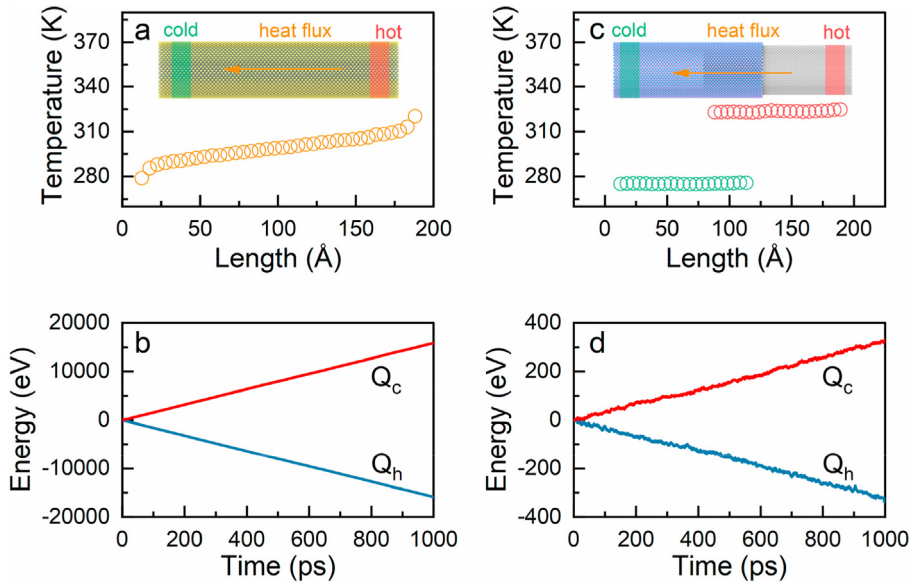

Fig. 2. NEMD simulations on the axial and interfacial thermal conductivity of nanotubes. (a) The temperature profile along the axial direction of CNT@MSNT and (b) corresponding accumulated energy changes in clod and hot regions used in the calculation of axial thermal conductivity. (c) The temperature profile along the axial direction of CNT@BNNT and (d) corresponding accumulated energy changes in clod and hot regions used in the calculation of interfacial thermal conductivity. Insets in (a) and (b) illustrate the corresponding simulation setups. (A colour version of this figure can be viewed online.)

transport can be reasonably ignored. Second, it is proven that the electrical conductivity of the CNT base is in the order of 10^5 S/m [47]. Thus, according to the Wiedemann-Franz law, the electronic thermal conductivity of CNTs is in the order of 1 W/mK [48], which is extremely smaller than the thermal conductivity originating from the phonons transport.

2.4. Calculations of interfacial thermal conductance

As shown in Fig. 2(c) and (d), we adopted a similar NEMD method to calculate the interfacial thermal conductance. In the calculations of interfacial thermal conductance, an artificial interface was created to make the heat flux J pass through the overlapping interface area A_1 between the inner and outer nanotubes, which results in a significant temperature difference dT. Thus, the interfacial thermal conductance G can be calculated from

$$G = \frac{J}{A_1 dT} \tag{3}$$

During the simulation, the whole structure was divided into five regions along the axial direction (see Fig. 2(c)), which is exactly similar to the treatment we conducted in the above thermal conductivity calculation. Here, the hot region with a length of 10 Å locates at the inner nanotube, while the cold region having the same length locates at the outer nanotube. The overlapping length between the inner CNT base and outer coating nanotubes was set as 4 nm. The interface area A_1 for all heterostructures was calculated as the surface area of overlapping inner CNT. After performing 500 ps relaxation simulations to achieve the steady heat flux transport, we calculated the temperature difference dT between inner and outer nanotubes by averaging the temperatures of the overlapping region in the subsequent 1000 ps simulations.

2.5. Calculations of vibrational density of states (VDOS)

The VDOS was studied to reveal the underlying mechanisms of phonon transport, which can be calculated from the Fourier transform of the velocity autocorrection function (VACF) [49].

$$VDOS(\nu) = \int \gamma(t) exp(-2\pi i \nu t) dt \tag{4}$$

where v denotes the frequency, i is the imaginary unit, and γ indicates the velocity autocorrelation function, which can be obtained from the equation 50 $\gamma(t) = \sum_i v_i(0) \cdot v_i(t) / \sum_i v_i(0) \cdot v_i(0)$ with vi(0) and vi(t) being the velocities of the ith atom at time t and at the initial state, respectively. Here, the VACF was calculated with a simulation run of over 10 ps after the structure has reached its equilibrium stage. In this simulation, the velocity information at each 10th time step was collected for calculating the VACF. Considering the fact that the nanotubes have a cylindrical structure, we decomposed the vibrations of nanotubes in the cylindrical coordinate system.51, 52 Specifically, the axial, radial, and azimuthal components of atomic velocities as shown in Figure S3 were, respectively, used to obtain the corresponding axial, radial, and azimuthal VDOS of nanotubes.

3. Results and discussion

3.1. Thermal transport in double-walled 1D vdW heterostructures

The (40,40) CNT-based vdW heterostructures are firstly considered here. The thermal conductivity and thermal conductance of various single-walled and double-walled nanotubes considered here are summarized in Table 1. Here, all nanotubes have the same length of 20 nm. As for the considered single-walled nanotubes, it is found that the CNT has the highest thermal conductivity, which is 630.75 W/mK for (40,40) CNT and 619.32 W/mK for (45,45) CNT, while the MSNT has the lowest thermal conductivity of 12.82 W/mK. The BNNT has a moderate thermal conductivity of 278.85 W/mK. The values of these three single-walled nanotubes are in good agreement with the previous studies based on NEMD methods [10,12,13]. As for the double-walled nanotubes, the thermal conductivities of CNT@CNT (i.e., the

Table 1
Thermal conductivity and thermal conductance of (40,40) CNT-based double-walled nanotubes and their nanotube components.

Nanotubes		R_{in}(Å)	R_{out}(Å)	A (Å^2)	K (W/mK)	σ (× 10^{-15} Wm/K)
Single-walled nanotubes	(40,40)CNT	27.31	/	590.28	630.75	3.723
	(45,45)CNT	30.72	/	663.99	619.32	4.112
	(45,45)BNNT	30.72	/	663.99	278.85	1.857
	(38,38)MSNT	32.43	/	1369.37	12.82	0.176
Double-walled nanotubes	(40,40)CNT@(45,45)CNT	27.31	30.72	1248.80	651.41	8.135
	(40,40)CNT@(45,45)BNNT	27.31	30.72	1248.80	406.48	5.078
	(40,40)CNT@(38,38)MSNT	27.31	32.43	1966.88	99.67	1.960

double-walled CNT), CNT@BNNT, and CNT@MSNT extracted from the present study are 651.41 W/mK, 406.48 W/mK, and 99.67 W/mK, respectively. Compared the thermal conductivity of double-walled nanotubes and their component layers, we found that the thermal conductivity of the double-walled CNT is identical to the value of its single-walled counterpart, while the thermal conductivity of CNT@BNNT (or CNT@MSNT) is between the values of their component CNT and BNNT (or MSNT) layers.

In addition to the thermal conductivity, we also calculated the thermal conductance as listed in Table 1 to eliminate the influence of cross-section area (see technical details in methods and modes). Moreover, to more clearly measure the contribution of the outer coating nanotube layer to the overall thermal conductance of 1D vdW heterostructures, we introduce the following parameter α:

$$\alpha = \frac{\sigma_{het} - \sigma_{in}}{\sigma_{in}} \tag{5}$$

where σ_{het} and σ_{in} are values of the thermal conductance of 1D vdW heterostructures and their inner CNT layer, respectively. If $\alpha > 0$, the outer coating nanotube layer can improve the thermal conductance of the structure, otherwise the coating nanotube layer has the opposite effect. As shown in Fig. 3, the values α are 1.18, 0.36, and −0.47 for CNT@CNT, CNT@BNNT, and CNT@MSNT, respectively. This result indicates that both CNT and BNNT coatings can improve the thermal transport property of 1D vdW heterostructures, while the MSNT coating has an opposite effect, which can reduce the thermal transport property. In addition to the parameter α, the parameter β having the following definition is introduced to evaluate the influence of interactions between neighboring nanotube layers on the thermal conductance of heterostructures:

$$\beta = \frac{\sigma_{het}}{\sum_i \sigma_i} \tag{6}$$

where σ_{het} is the thermal conductance of heterostructure and σ_i denotes the thermal conductance of the ith isolated nanotube component. For double-walled nanotubes, $\sum_i \sigma_i$ is the sum of the thermal conductance of isolated inner CNT base and outer nanotube coating. As shown in Fig. 3, the values of β for CNT@CNT, CNT@BNNT, and CNT@MSNT are 1.04, 0.91, and 0.50, respectively. These results indicate that the thermal conductance of CNT@CNT is slightly higher than the sum of the values of the inner CNT base and the outer CNT coating, which is thus twice the value of the single-walled CNT. The value of CNT@BNNT is close to but slightly lower than the sum of the values of the inner CNT and the outer BNNT, which is thus still significantly higher than the value of the single-walled CNT. The different enhancement effects of CNT and BNNT coatings on the thermal conductivity of CNT base can be understood by the fact that the CNT has a thermal conductivity much higher than that of BNNT. Besides, the mass of nitrogen and boron atoms is different from that of the carbon atom. This difference can result in an acoustic mismatch between the inner CNT and outer BNNT in CNT@BNNT, which can be regarded as another factor responsible for the above result that the thermal conductance of CNT@BNNT is slightly lower than the sum of the values of its inner CNT and outer BNNT components. The enhanced thermal conductance observed in CNT@CNT and CNT@BNNT is in accordance with our expectation since an outer coating layer can provide an additional heat conducting path [14]. However, different from CNT@CNT and CNT@BNNT, a reduced thermal conductance is found in CNT@MSNT, which is only about one half of the value of the single-walled CNT. This unexpected reduction in the thermal conductance of CNT@MSNT will be explained in detail later.

To explain the different effects of different nanotube coatings on the overall thermal conductance of the corresponding 1D vdW heterostructures, we show their temperature distribution in Fig. 4(a)-(c) as well as their cumulative energy change in Fig. 4(d)–(f). The corresponding results of the inner and outer nanotube components in these 1D vdW heterostructures are also

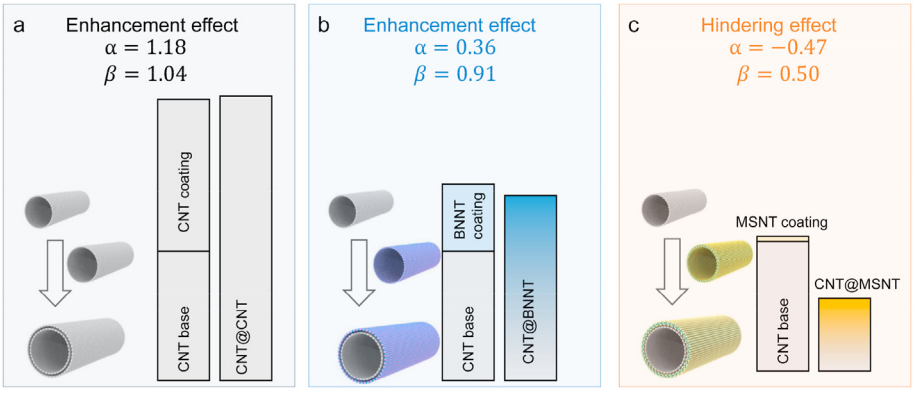

Fig. 3. Effects of (a) CNT, (b) BNNT, and (c) MSNT coating layers on the thermal conductance of different (40,40) CNT-based double-walled nanotubes. The height of each rectangle denotes the relative magnitude of the corresponding thermal conductance. (A colour version of this figure can be viewed online.)

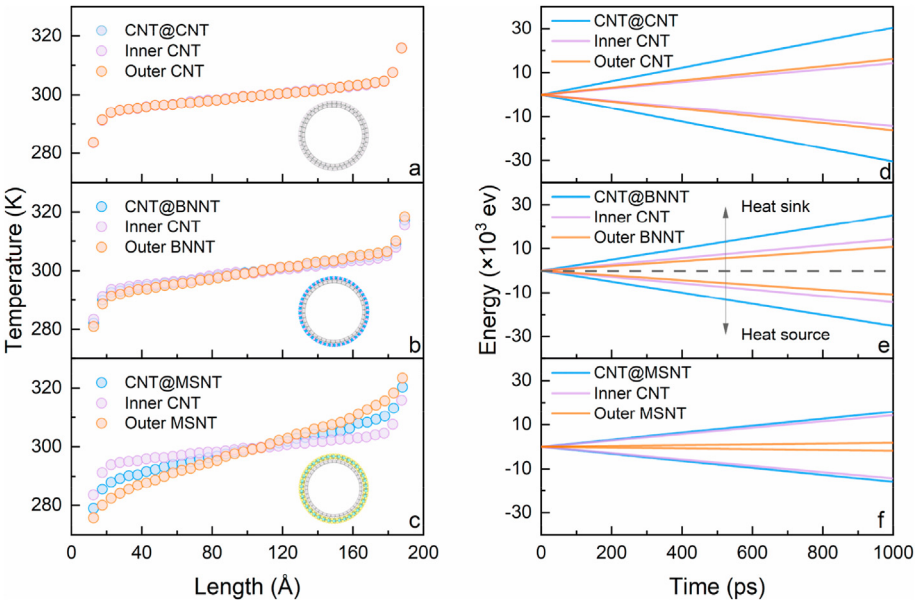

Fig. 4. (a–c) The temperature profiles along the axial direction of (40,40) CNT-based double-walled nanotubes including CNT@CNT, CNT@BNNT, and CNT@MSNT. The temperature distribution of each component in these nanotubes is also shown here. (d–f) The accumulated energy changes in the heat sink and source in CNT@CNT, CNT@BNNT, and CNT@MSNT. It is noted that isolated inner and outer nanotubes are used here to calculate the energy changes. (A colour version of this figure can be viewed online.)

shown here for the sake of comparison. A dramatic temperature drop near the heat source and the sink region is found in all calculated structures, which can be attributed to the unavoidable intensive phonon scattering. Under this circumstance, only the linear temperature distribution region ranging from 30 Å to 170 Å was considered in the calculation of the temperature gradient. The cumulative energy changes in the heat source and sink region are identical to each other, which increase linearly with respect to the growing simulation time.

The temperature gradients of CNT@CNT and its two component layers extracted from Fig. 4(a) are 0.060 K/Å (CNT@CNT), 0.059 K/Å (inner layer), and 0.061 K/Å (outer layer). Meanwhile, as shown in Fig. 4(d), the heat flows of these structures are 30.6 eV/ps (CNT@CNT), 14.4 eV/ps (inner layer), and 16.2 eV/ps (outer layer). Based on these results, we can see that the temperature gradient of CNT@CNT is identical to the results of their component CNT layers, while the heat flux of CNT@CNT is equal to the sum of values of the inner and outer CNTs, which leads to the enhanced thermal conductance observed in CNT@CNT as shown in Fig. 3(a). Similarly, the heat flux of CNT@BNNT shown in Fig. 4(b) is also the sum of the values of its inner and outer nanotubes. However, the temperature gradient of CNT@BNNT is between the values of its inner CNT and outer BNNT components. This fact accounts for the slight discrepancy of the thermal conductance of CNT@BNNT from the sum of the values of its inner CNT and outer BNNT components as shown in Fig. 3(b). Similar to CNT@CNT and CNT@BNNT, the heat flow of CNT@MSNT is greatly increased, which is nearly equal to the sum of the values of its inner CNT and outer MSNT components (see Fig. 4(c)) even though this increment is much smaller than the improvement in CNT@CNT and CNT@BNNT. On the other hand, different from CNT@CNT and CNT@BNNT, the temperature gradient of CNT@MSNT is found to be greatly larger than the value of its inner CNT layer (see Fig. 4(f)). The greatly increased temperature gradient of CNT@MSNT due to coating of the outer MSNT layer is thus responsible for the reduced thermal conductance of CNT@MSNT observed in Fig. 3(c).

From the above results of double-walled CNTs and two 1D vdW heterostructures, we can see that the outer nanotube coating can affect the thermal conductance of 1D vdW heterostructures by changing the heat flux and the temperature gradient. Specifically, the coating nanotube provides an additional heat-conducting path that can enhance the thermal conductance, while the temperature gradient can be increased due to the coating of outer nanotube, which can reduce the thermal conductance. The competition between these two factors results in different effects of coating nanotube materials on the thermal conductance of 1D vdW heterostructures. For example, in CNT@CNT and CNT@BNNT, the change in the thermal conductance is predominated by the enhancement in heat flux, while the enhancement in temperature gradient turns to be the dominant factor in CNT@MSNT.

The VDOS of inner and outer nanotubes in double-walled CNTs and two 1D vdW heterostructures are compared in Fig. 5 to further provide microscopic insight into the enhancement/hindering effects of different coating nanotubes on the thermal conductance of 1D vdW heterostructures. Here, as mentioned before, the axial VDOS is based on the VACF along the tube axis, i.e., axial direction, while the radial and azimuthal VDOS is, respectively, based on the VACF along the radial and azimuthal directions of the cross-section of nanotubes. It is found that as for these three VDOS modes, the overlapping area between the inner CNT and outer nanotube layer follows the order CNT@CNT > CNT@BNNT > CNT@MSNT, which indicates no, weak and strong interfacial phonon scattering in them, respectively. The diversity of phonon overlaps of these nanotubes are attributed to their different lattice structures. For example, BNNT has a lattice structure extremely analog to that of CNT though the relative atomic mass of boron and nitrogen is slightly different from that of carbon. As shown in Fig. 5, BNNT and CNT layers almost have the same distribution of VDOS, despite that the radial VDOS of BNNT has a lower frequency than that of CNT. However, when compared to BNNT and CNT, MSNT has a more complicated atomic structure, in which each molybdenum atom is surrounded by six sulfur atoms. In other words, a molybdenum atom layer in MSNT is sandwiched by two sulfur atom layers [53]. Moreover, the relative atomic mass of molybdenum is greatly larger than that of carbon. These differences lead to the VDOS of MSNT significantly different from that of CNT. Specifically, as shown in

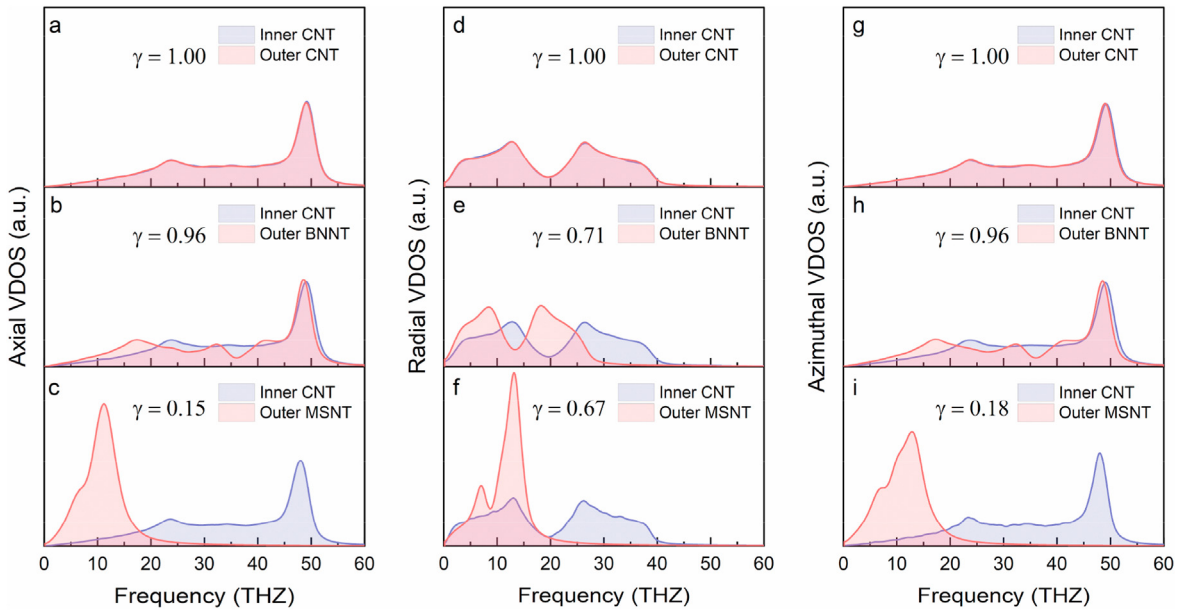

Fig. 5. The axial, radial and azimuthal VDOS of inner and outer nanotube components of (40,40) CNT-based double-walled nanotubes including CNT@CNT (top), CNT@BNNT (middle), and CNT@MSNT (bottom). (A colour version of this figure can be viewed online.)

Fig. 5(c), (f), and (i), the frequency of VDOS of MSNT is much smaller than that of its CNT counterpart.

To further quantify the overlap in VDOS, we calculate the following similarity index γ [54–56].

$$\gamma = \frac{\int f(T)g(T)dT}{\sqrt{\int f^2(T)dT \int g^2(T)dT}} \tag{7}$$

which is a measure of the correlation between spectra $f(T)$ and $g(T)$ in a certain frequency range. The calculated γ of CNT@CNT, CNT@BNNT, and CNT@MSNT along three different directions is plotted in Fig. 5. After averaged in three directions, the values of γ for CNT@CNT, CNT@BNNT, and CNT@MSNT are 1.00, 0.88, and 0.33, respectively. As plotted in Figure S4 in the supplementary materials, we find that parameter β of different 1D vdW heterostructures increases linearly with their γ. This result indicates that the change in the thermal conductance of 1D vdW heterostructures depends on the phonon scattering between the inner CNT base and the outer nanotube coating layers. In other words, the stronger phonon scattering will result in a larger decrease in the thermal conductance of heterostructures.

In Fig. 6(a)-(c), we show the thermal conductance of CNT@CNT, CNT@BNNT, and CNT@MSNT with different effective lengths in the heat flux direction. The results of their component layers are also shown here. The effective length denotes the linear region of temperature distribution as plotted in Fig. 2(a). Thus, the nanotubes with a length ranging from 10 nm to 50 nm have an effective length ranging from 6.2 nm to 43.6 nm. Based on the results shown in Fig. 6(a)–(c), we calculated the parameter α of nanotubes with different effective lengths, whose values are graphically shown in Fig. 6(d)–(f). From Fig. 6(d)-(f) we can see that due to the boundary effect, the factor α of all double-walled nanotubes change with growing effective length L. Specifically, when L increases from 6.2 nm to 43.6 nm, α of CNT@BNNT and CNT@MSNT is found to, respectively, increase from 0.48 and −0.57 to 0.36 and −0.31. In the same process, α of CNT@CNT is found to grow from 1.03 to 1.19. According to the kinetic theory [45], the phonons transport in low-dimensional materials will transform from ballistic regime to diffusive regime with increasing length, which results in the increase of thermal conductivity in this process until approaching a constant value. The length-dependent thermal conductance can be expressed as [57,58].

$$\sigma = \frac{\sigma_\infty}{\left(\frac{l_p}{L} + 1\right)} \tag{8}$$

where σ_∞ is the length-independent thermal conductance of nanotubes with the infinite length, and l_p is the effective phonon mean free path. The thermal conductance σ of all nanotubes is graphically shown in Fig. 6 as a function of the length L. The thermal conductance of all nanotubes is found to increases as their L grows. By fitting Eq. (6) to our NEMD results shown in Fig. 6(a)–(c), the values of σ_∞ can be obtained, which are listed in Table 2. With the aid of σ_∞ the corresponding length-independent values of k and α, i.e., k_∞ and α_∞ can be calculated, which are also listed in Table 2. As shown in Table 2, the values of α_∞ are 1.24, 0.32, and −0.11 for CNT@CNT, CNT@BNNT, and CNT@MSNT, respectively. Although the length-independent α_∞ is found to slightly smaller or larger than α of a nanotube with the finite length, α and its corresponding α_∞ are found to have the same sign. This result indicates that the effect of coating layer on the thermal transport in the nanotubes with an infinite length is qualitatively similar to that on the structures with a finite length, though a small quantitative difference is observed between the nanotubes with finite and infinite lengths.

In the above discussion, we have considered the double-walled nanotubes with (40,40) CNT base. To investigate the effects of chirality and radius on the thermal transport in CNT-based heterostructures, we perform the similar NEMD simulations on CNT@CNT, CNT@BNNT, and CNT@MSNT structures with zigzag (70,0) CNT base, armchair (20,20) CNT base and chiral (60,30) CNT base. All structures have the same length of 20 nm. Meanwhile, the outer nanotube coatings in heterostructures have the same chirality as that of the CNT base. It is noted that the radius of (70,0) CNT base (27.59 Å) is very close to the above (40,40) CNT base (27.31 Å), while the radius of (60,40) CNT base (31.29 Å) is slightly

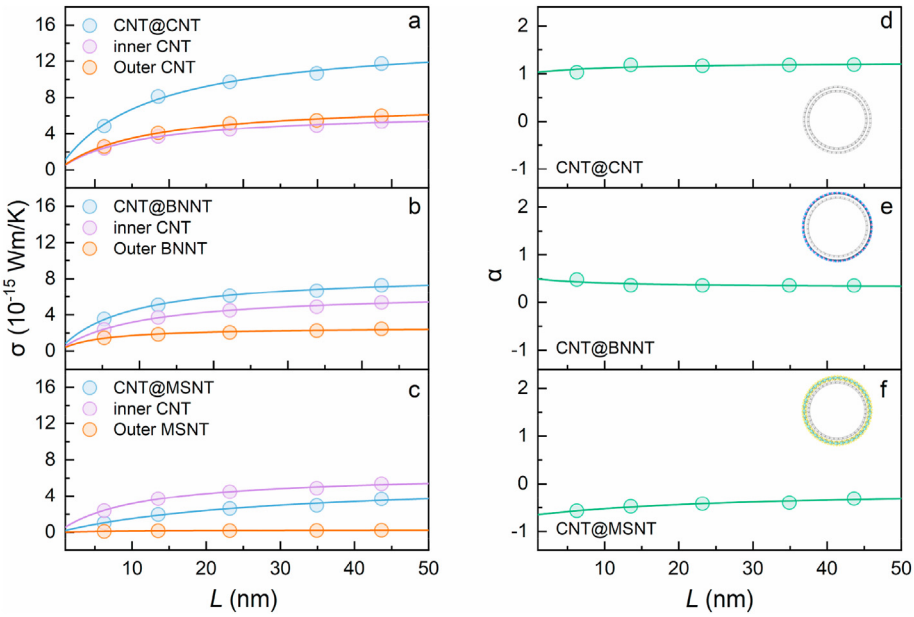

Fig. 6. Length-dependent thermal conductance σ (left) and parameter α (right) of (40,40) CNT-based double-walled nanotubes including CNT@CNT (top), CNT@BNNT (middle), and CNT@MSNT (bottom). The circles and lines are results obtained from NEMD simulations and fitted by Eq. (6), respectively. (A colour version of this figure can be viewed online.)

Table 2
Length-independent thermal conductivity k_∞, thermal conductance σ_∞, and parameter α_∞ of the simulated nanotubes by fitting Eq (6) to results extracted from NEMD simulations.

Nanotubes		k_∞(W/mK)	σ_∞ ($\times 10^{-15}$ Wm/K)	α_∞
Single-walled nanotubes	(40,40)CNT	1110.82	6.557	/
	(45,45)CNT	1130.44	7.506	/
	(45,45)BNNT	397.60	2.640	/
	(38,38)MSNT	19.84	0.272	/
Double-walled nanotubes	(40,40)CNT@(45,45)CNT	1178.73	14.720	1.24
	(40,40)CNT@(45,45)BNNT	690.58	8.624	0.32
	(40,40)CNT@(38,38)MSNT	295.49	5.812	−0.11

larger than but also close to that of (40,40) CNT base. The obtained thermal conductance and thermal conductivity of (70,0) CNT, (20,20) CNT, and (60,30) CNT-based double-walled nanotubes are, respectively, listed in Tables S1–S3 in the supplementary materials, while values of the corresponding α and β of these structures are plotted in Figures S5–S7. A detailed comparison of α and β among different 1D vdW heterostructures is illustrated in Figure S8. In general, it is found that despite some slight quantitative differences observed among the structures with (40,40) CNT, (20,20) CNT, (70,0) CNT, and (60,30) CNT bases, the effect of the coating layer on the thermal transport properties of heterostructures with different CNT bases is very close to each other. In other words, the coating layer is found to have the similar effect on the thermal transport in 1D vdW heterostructures with different radii and chiralities.

3.2. Thermal transport in triple-walled 1D vdW heterostructures

In addition to the aforementioned 1D vdW heterostructures containing two layers, 1D vdW heterostructures with three component layers are also observed in experiments [6]. In this section, taking (40,40) CNT-based heterostructure, i.e., CNT@BNNT@MSNT with the length of 20 nm as an example (see Fig. 7(a)), we investigate the thermal transport in 1D vdW heterostructures composed of three layers of nanotubes. By obtaining the temperature gradient from the linear region of temperature distribution shown in Fig. 7(b) and the cumulative energy change shown in Fig. 7(c), the thermal conductivity and thermal conductance are calculated as 52.873 W/mK and 1.447 $\times$ 10^{-15} Wm/K, respectively. The corresponding factor α is thus obtained as −0.61, indicating a 61% reduction in the thermal conductance, which is larger than 47% of CNT@MSNT. This indicates that the outer coating layers of CNT@BNNT@MSNT have a greater reduction effect on the thermal transport property of the CNT base, which is in contrast to our expectation since it is expected that the thermal conductance of CNT@BNNT@MSNT should be smaller than that of CNT@BNNT but larger than that of CNT@MSNT. To explain this discrepancy, we calculate the heat flux and the temperature distribution of CNT@BNNT@MSNT.

The temperature distribution of CNT@BNNT@MSNT together with the results of its three nanotube components is plotted in Fig. 7(b). From this figure, we find that the temperature gradient of CNT@BNNT@MSNT is 0.0875 K/Å, which is between the values of its middle BNNT (0.0523 K/Å) and outer MSNT (0.1633 K/Å) layers, and is much larger than the value of its inner CNT layer (0.0280 K/Å). Similar to the above 1D vdW heterostructures with two layers, the difference in the temperature gradient of three nanotube components of CNT@BNNT@MSNT can be explained by their VDOS distributions in Fig. 7(d), which show the diversity of phonon overlaps owing to their different lattice structures. As plotted in Fig. 7(c), the total heat flux of CNT@BNNT@MSNT is 7.9 eV/ps, which is smaller than the values of its isolated inner CNT (14.4 eV/ps) and middle BNNT (10.8 eV/ps) layers, but is much larger than the value of its

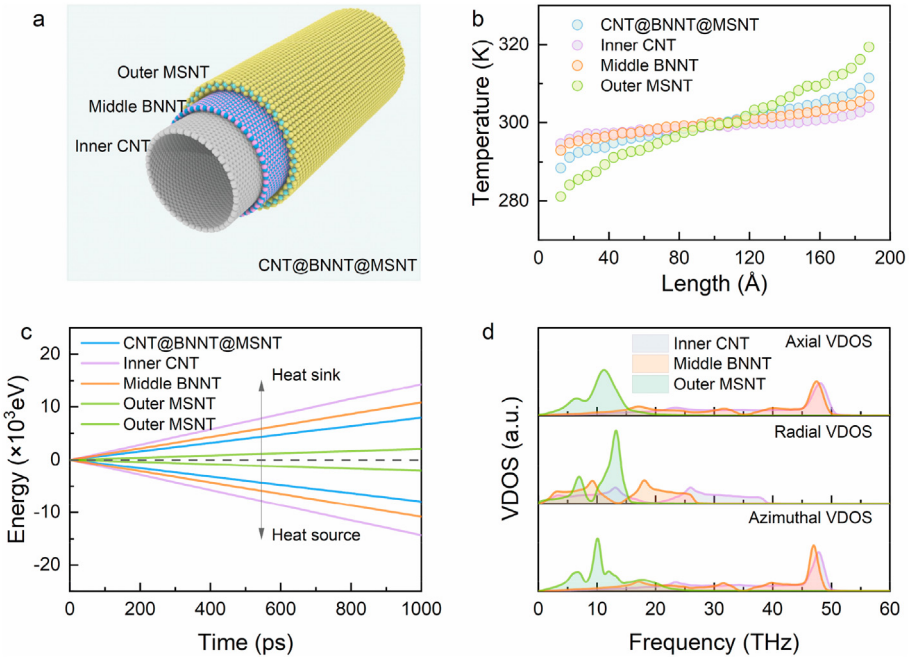

Fig. 7. (a) The atomic structure of CNT@BNNT@MSNT heterostructure. (b) Temperature profile and accumulated energy change in CNT@BNNT@MSNT and their component layers. (d) The axial (top), radial (middle), and azimuthal (bottom) VDOS of each component layer of CNT@BNNT@MSNT. (A colour version of this figure can be viewed online.)

isolated outer MSNT (2.1 eV/ps) layer. As for its counterparts with two layers, i.e., CNT@CNT, CNT@BNNT and CNT@MSNT, the heat flux, however, is found to be very close to the sum of the values of its inner and outer nanotubes (see Fig. 4(d)–(f)). Hence, the suppression of heat flux in CNT@BNNT@MSNT is responsible for the significant reduction in its thermal conductivity.

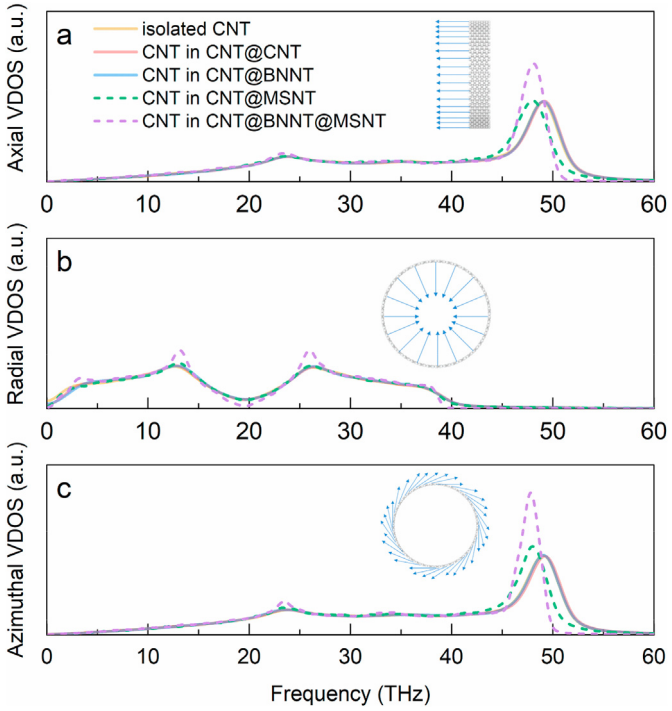

Fig. 8. The (a) axial, (b) radial, and (c) azimuthal VDOS of the (40,40) CNT base in CNT@CNT, CNT@BNNT, CNT@MSNT, and CNT@BNNT@MSNT. Here, the isolated CNT is also considered for the sake of comparison. The insets show the components of atomic velocities used to calculate the corresponding phonon modes. (A colour version of this figure can be viewed online.)

To better understand the reduced heat flux observed in CNT@BNNT@MSNT, in Fig. 8 we compare axial, radial, and azimuthal VDOS of the CNT layer in different 1D vdW heterostructures. For the sake of comparison, the corresponding value of an isolated CNT is also shown in Fig. 8. For the axial and azimuthal VDOS, it is found that the VODS of inner CNT of CNT@CNT and CNT@BNNT is identical to that of the isolated CNT, whose highest peaks are all around 49 THz. However, as for the inner CNT of CNT@MSNT, the peak of VDOS slightly moves downwards to ~48 THz. The VDOS of the inner CNT of CNT@BNNT@MSNT similarly has the highest peak around 48 THz. However, the intensity of the same phonon peaks of CNT@BNNT@MSNT is greatly increased, especially for the azimuthal VDOS at the high frequency regime from 45 THz to 50 THz. For the radial VDOS, the configuration of inner CNT under BNNT@MSNT coating is different from other counterparts, owning a shark phonon peak around 12 THz and 26 THz. These increased phonon peaks at high frequency regime can be attributed to the possible compression existing on the inner CNT layer, similar to a solid under pressure loading [59,60]. This compression can be understood by the fact that in CNT@BNNT@MSNT, the inner CNT layer is constrained by double-layered BNNT-MSNT, which thus can more significantly suppress the vibration of inner CNT when compared with its counterpart in CNT@CNT, CNT@BNNT, and CNT@MSNT. This explains the origin of the suppressed heat flux and the reduced thermal conductance in CNT@BNNT@MSNT.

In addition to CNT@BNNT@MSNT, we have also performed the similar NEMD simulations on CNT@MSNT@BNNT (see Figure S9 in the supplementary materials) to investigate the influence of the sequence of BNNT and MSNT coatings on the thermal conductance of CNT-based triple-walled heterostructures. The thermal conductance of CNT@MSNT@BNNT is 1.76×10^{-15} Wm/K, corresponding to a 53% reduction in the thermal conductance when compared to the isolated CNT. This 53% reduction in the thermal conductance of CNT@MSNT@BNNT is close to but slightly smaller than the 61% reduction observed in its CNT@BNNT@MSNT counterpart. Similar

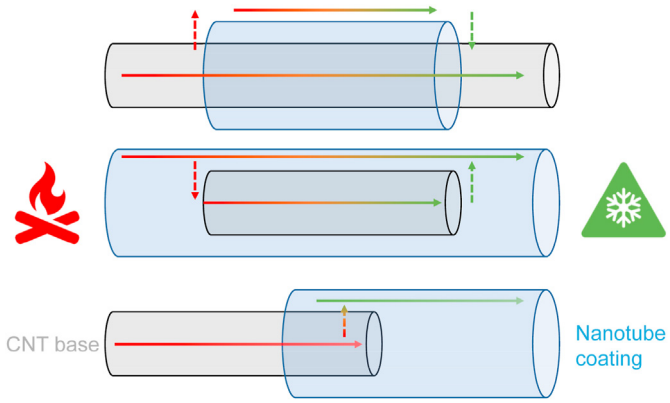

Fig. 9. Schematic illustration of heat transport in 1D vdW heterostructures. The solid lines and dotted lines denote heat transport along the axial direction and through the interface between the CNT base and nanotube coating, respectively. Three representative models are plotted here. Specifically, the bottom one is employed to calculate the interfacial thermal conductance by the NEMD method. (A colour version of this figure can be viewed online.)

to CNT@BNNT@MSNT, the reduced thermal conductance observed in CNT@MSNT@BNNT can be attributed to its reduced heat flux. As shown in Figure S6, the total heat flux (8.505 eV/ps) of CNT@BNNT@MSNT is much smaller than the value of its isolated inner CNT (14.4 eV/ps) and outer BNNT (13.45 eV/ps) layers, indicating the suppression of the heat flux in CNT@BNNT@MSNT. Since the BNNT layer can transfer the heat much faster than the MSNT layer, the thermal conductance of CNT@MSNT@BNNT is expected to be larger than that of CNT@BNNT@MSNT, because in CNT@MSNT@BNNT the BNNT layer has a much larger volume ratio. As a result, compared to CNT@BNNT@MSNT, the coating layers should have a weaker hindering effect on the thermal transport properties of CNT@MSNT@BNNT. This prediction is consistent with the NEMD results shown above.

3.3. Interfacial thermal transport in 1D vdW heterostructures

As mentioned above, the 1D vdW heterostructures have promising potentials in nanoscale thermal management and thermal circuits. As illustrated in Fig. 9, in 1D vdW heterostructures thermal can not only transport along the axial direction but also go through the interface between CNT base and nanotube coating. Thus, to achieve a better understanding of the heat dissipation mechanism in 1D vdW heterostructures, it becomes important to investigate the thermal conductance at the interface between adjunct nanotube layers. To this end, the interfacial thermal conductance of two 1D vdW heterostructures, i.e., (40,40) CNT-based heterostructures including CNT@BNNT and CNT@MSNT is calculated. Moreover, CNT@CNT is also considered here for the sake of comparison. In Fig. 10, we show the interfacial temperature difference and the heat flux in CNT@CNT, CNT@BNNT, and CNT@MSNT. Here, all structures are assumed to have the same overlapping area. It is found that the interfacial temperature differences in CNT@CNT, CNT@BNNT, and CNT@MSNT are, respectively, 46.64 K, 47.53 K, and 43.37 K, while their heat fluxes are 0.863 eV/ps, 0.322 eV/ps, and 0.107 eV/ps, respectively. From these results, we can see that there is no significant temperature gradient existing in the inner and outer nanotube layers of CNT@CNT and CNT@BNNT since their thermal conductance along the axial direction is much larger than that along the interface direction. On the contrary, a significant temperature gradient is observed in the outer MSNT layer of CNT@MSNT, which is owing to its relatively low axial thermal conductance of MSNT.

According to Eq. (3), values of the interfacial thermal conductance of CNT@CNT, CNT@BNNT, and CNT@MSNT are calculated, which are 4.323 MW/m^{2}K, 1.584 MW/m^{2}K, and 0.578 MW/m^{2}K, respectively. The interfacial thermal conductance of CNT@CNT is about three times larger than that of CNT@BNNT and is about seven times larger than that of CNT@MSNT. The different values of the interfacial thermal conductance observed in different structures can be explained by different phonon coupling modes as detailed above, in which the VDOS of the component layers of CNT@CNT, CNT@BNNT, and CNT@MSNT, respectively, is completely, highly, and scantly overlapped. In contrast to their high thermal conductivity along the axial direction, the weak interface heat transport properties can be a drawback of 1D vdW heterostructures in the nanoelectronics applications, since they are hard to dissipate heat to surroundings through their interfaces.

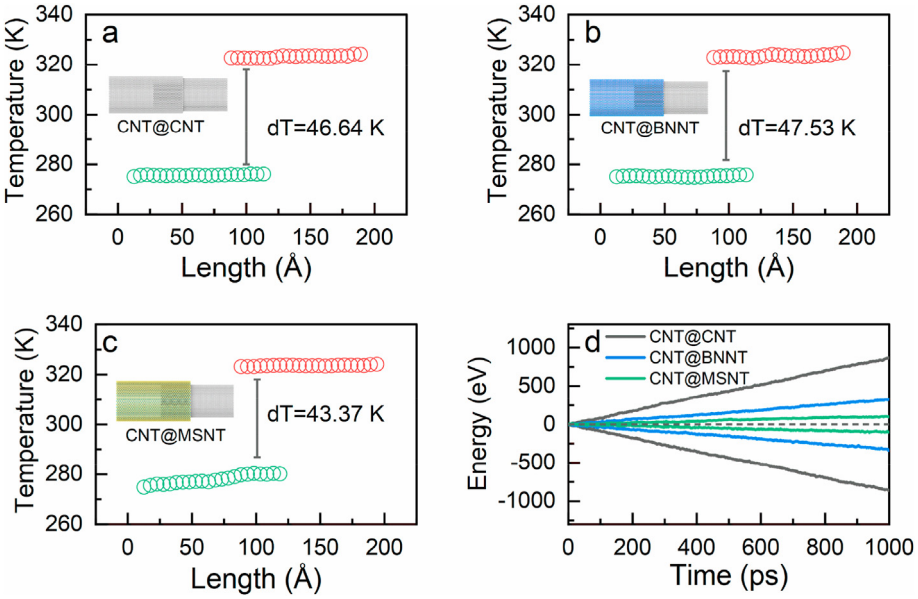

Fig. 10. Temperature profiles of (40,40) CNT-based double-walled nanotubes including (a) CNT@CNT, (b) CNT@BNNT, and (c) CNT@MSNT along the axial direction. (d) The corresponding accumulated energy changes in cold and hot regions in these nanotube structures. (A colour version of this figure can be viewed online.)

4. Conclusions

In this paper, the axial and interfacial thermal transport behaviors of 1D vdW heterostructures are investigated by using NEMD simulations. As for the axial thermal conductance of (40,40) CNT-based 1D vdW heterostructures containing two component layers, i.e., CNT@BNNT and CNT@MSNT, it is found that the BNNT coating layer in CNT@BNNT can increase the thermal conductance by 36%. This result is similar to the enhancement effect observed in the double-walled CNT, i.e., CNT@CNT though a CNT coating can increase the thermal conductance by 118%. Different from CNT@CNT and CNT@BNNT, the MSNT coating layer in CNT@MSNT has an opposite effect, which can reduce the thermal conductance by 47%. The different enhancement/hindering effects of different coating layers on the thermal conductance of different 1D vdW heterostructures are attributed to the competition between improved heat flux and increased temperature gradient due to outer nanotube coatings, since inner CNT and outer nanotube may have different lattice structures and also different relative atomic masses, both of which can result in varied VDOS overlapping degree in different 1D vdW heterostructures. The interfacial thermal conductance of CNT@CNT, CNT@BNNT, and CNT@MSNT is also examined to provide a better understanding of the heat dissipation mechanism in 1D vdW heterostructures.

In addition to 1D vdW heterostructures containing two layers, we also investigate the thermal transport behaviors of their counterparts containing three layers, i.e., CNT@BNNT@MSNT. An unexpected reduction of 61% is observed in the thermal conductance of this 1D vdW heterostructure, which is even larger than the reduction of 47% observed in the thermal conductance of CNT@MSNT. Such a significant reduction of thermal conductance observed in CNT@BNNT@MSNT is caused by the suppressed heat flux due to the vibration suppression by two outer nanotube layers.

Declaration of competing interest

There are no conflicts to declare.

Acknowledgments

This study was supported by the National Key R&D Program of China (No. 2018YFB1502602) and the National Natural Science Foundation of China (Nos. 11932005, 11772106). The authors thank Dr. Zheyong Fan of Aalto University and Mr. Xu Zhang of Harbin Institute of Technology, Shenzhen for discussions and insightful comments.

Appendix A. Supplementary data

Supplementary data to this article can be found online at https://doi.org/10.1016/j.carbon.2021.01.146.

References

[1] K.S. Novoselov, A. Mishchenko, A. Carvalho, A.H.C. Neto, 2D materials and van der Waals heterostructures, Science 353 (6298) (2016) aac9439.
[2] F. Withers, O. Del Pozo-Zamudio, A. Mishchenko, A.P. Rooney, A. Gholinia, K. Watanabe, et al., Light-emitting diodes by band-structure engineering in van der Waals heterostructures, Nat. Mater. 14 (3) (2015) 301–306.
[3] X.P. Hong, J. Kim, S.F. Shi, Y. Zhang, C.H. Jin, Y.H. Sun, et al., Ultrafast charge transfer in atomically thin MoS_2/WS_2 heterostructures, Nat. Nanotechnol. 9 (9) (2014) 682–686.
[4] T. Georgiou, R. Jalil, B.D. Belle, L. Britnell, R.V. Gorbachev, S.V. Morozov, et al., Vertical field-effect transistor based on graphene-WS_2 heterostructures for flexible and transparent electronics, Nat. Nanotechnol. 8 (2) (2013) 100–103.
[5] Y. Gogotsi, B.I. Yakobson, Nested hybrid nanotubes, Science 367 (6477) (2020) 506–507.
[6] R. Xiang, T. Inoue, Y.J. Zheng, A. Kumamoto, Y. Qian, Y. Sato, et al., One-dimensional van der Waals heterostructures, Science 367 (6477) (2020) 537–542.
[7] M.G. Burdanova, R.J. Kashtiban, Y.J. Zheng, R. Xiang, S. Chiashi, J.M. Woolley, et al., Ultrafast optoelectronic processes in 1d radial van der waals heterostructures: carbon, boron nitride, and MoS_2 nanotubes with coexisting excitons and highly mobile charges, Nano Lett. 20 (5) (2020) 3560–3567.
[8] S. Kaur, N. Raravikar, B.A. Helms, R. Prasher, D.F. Ogletree, Enhanced thermal transport at covalently functionalized carbon nanotube array interfaces, Nat. Commun. 5 (1) (2014) 3082.
[9] Z. Yao, J.-S. Wang, B. Li, G.-R. Liu, Thermal conduction of carbon nanotubes using molecular dynamics, Phys. Rev. B 71 (8) (2005), 085417.
[10] R.N. Salaway, L.V. Zhigilei, Molecular dynamics simulations of thermal conductivity of carbon nanotubes: resolving the effects of computational parameters, Int. J. Heat Mass Tran. 70 (2014) 954–964.
[11] T.T. He, T. Li, Z.X. Huang, Z.A. Tang, X.Y. Guan, Mechanical and thermal properties of the coaxial carbon nanotube@boron nitride nanotube composite, Phys. E Low-dimens. Syst. Nanostruct. 107 (2019) 182–186.
[12] S.Q. Li, W.H. Qi, S.Y. Xiong, D.Q. Yu, Thermal conductivity of single-wall MoS_2 nanotubes, Appl. Phys. Mater. Sci. Process 124 (3) (2018) 218.
[13] H. Meng, D.K. Ma, X.X. Yu, L.F. Zhang, Z.J. Sun, N. Yang, Thermal conductivity of molybdenum disulfide nanotube from molecular dynamics simulations, Int. J. Heat Mass Tran. 145 (2019), 118719.
[14] L. Jing, M.K. Samani, B. Liu, H. Li, R.Y. Tay, S.H. Tsang, et al., Thermal conductivity enhancement of coaxial carbon@boron nitride nanotube arrays, ACS Appl. Mater. Interfaces 9 (17) (2017) 14555–14560.
[15] P. Wang, Y. Zheng, T. Inoue, R. Xiang, A. Shawky, M. Watanabe, et al., Enhanced in-plane thermal conductance of thin films composed of coaxially combined single-walled carbon nanotubes and boron nitride nanotubes, ACS Nano 14 (4) (2020) 4298–4305.
[16] Z.P. Xu, M.J. Buehler, Heat dissipation at a graphene-substrate interface, J. Phys. Condens. Matter 24 (47) (2012), 475305.
[17] Y. Huang, J. Wu, K.C. Hwang, Thickness of graphene and single-wall carbon nanotubes, Phys. Rev. B 74 (24) (2006), 245413.
[18] P.H. Ying, Y.F. Zhao, H.F. Tan, Study on collapse controlling of single-wall carbon nanotubes by helium storage, Comput. Mater. Sci. 164 (2019) 133–138.
[19] B.-Y.C. Ji-Hang Zou, Phonon thermal properties of graphene on h-BN from molecular dynamics simulations, Appl. Phys. Lett. 110 (10) (2017).
[20] J.C. Zhang, Y. Hong, Y.A. Yue, Thermal transport across graphene and single layer hexagonal boron nitride, J. Appl. Phys. 117 (13) (2015).
[21] J.W. Jiang, H.S. Park, Mechanical properties of MoS_2/graphene heterostructures, Appl. Phys. Lett. 105 (3) (2014), 033108.
[22] S. Srinivasan, G. Balasubramanian, Reduced thermal transport in the graphene/MoS_2/graphene heterostructure: a comparison with freestanding monolayers, Langmuir 34 (10) (2018) 3326–3335.
[23] Y. Ma, Y. Dai, M. Guo, C. Niu, B. Huang, Graphene adhesion on MoS_2 monolayer: an ab initio study, Nanoscale 3 (9) (2011) 3883–3887.
[24] S. Haastrup, S. Latini, K. Bolotin, K.S. Thygesen, Stark shift and electric-field-induced dissociation of excitons in monolayer MoS_2 and hBN/MoS_2heterostructures, Phys. Rev. B 94 (4) (2016), 041401.
[25] R.H. Miwa, W.L. Scopel, Lithium incorporation at the MoS_2/graphene interface: an ab initio investigation, J. Phys. Condens. Matter 25 (44) (2013), 445301.
[26] A. Stukowski, Visualization and analysis of atomistic simulation data with OVITO–the Open Visualization Tool, Model. Simulat. Mater. Sci. Eng. 18 (1) (2010), 015012.
[27] S. Plimpton, Fast parallel algorithms for short-range molecular-dynamics, J. Comput. Phys. 117 (1) (1995) 1–19.
[28] P. Boone, H. Babaei, C.E. Wilmer, Heat flux for many-body interactions: corrections to LAMMPS, J. Chem. Theor. Comput. 15 (10) (2019) 5579–5587.
[29] T. Schneider, E. Stoll, Molecular-dynamics study of a three-dimensional one-component model for distortive phase transitions, Phys. Rev. B 17 (3) (1978) 1302.
[30] L. Lindsay, D. Broido, Optimized Tersoff and Brenner empirical potential parameters for lattice dynamics and phonon thermal transport in carbon nanotubes and graphene, Phys. Rev. B 81 (20) (2010), 205441.
[31] A. Kınacı, J.B. Haskins, C. Sevik, T. Çağın, Thermal conductivity of BN-C nanostructures, Phys. Rev. B 86 (11) (2012), 115410.
[32] T. Liang, S.R. Phillpot, S.B. Sinnott, Parametrization of a reactive many-body potential for Mo-S systems, Phys. Rev. B 79 (24) (2009), 245110.
[33] J.A. Stewart, D.E. Spearot, Atomistic simulations of nanoindentation on the basal plane of crystalline molybdenum disulfide (MoS_2), Model. Simulat. Mater. Sci. Eng. 21 (4) (2013), 045003.
[34] K. Xu, A.J. Gabourie, A. Hashemi, Z.Y. Fan, N. Wei, A.B. Farimani, et al., Thermal transport in MoS_2 from molecular dynamics using different empirical potentials, Phys. Rev. B 99 (5) (2019), 054303.
[35] J.-W. Jiang, H.S. Park, T. Rabczuk, Molecular dynamics simulations of single-layer molybdenum disulphide (MoS_2): Stillinger-Weber parametrization, mechanical properties, and thermal conductivity, J. Appl. Phys. 114 (6) (2013), 064307.
[36] A. Kandemir, H. Yapicioglu, A. Kinaci, T. Çağın, C. Sevik, Thermal transport properties of MoS_2 and $MoSe_2$ monolayers, Nanotechnology 27 (5) (2016), 055703.
[37] L.A. Girifalco, M. Hodak, R.S. Lee, Carbon nanotubes, buckyballs, ropes, and a universal graphitic potential, Phys. Rev. B 62 (19) (2000) 13104–13110.

[38] S.L. Mayo, B.D. Olafson, W.A. Goddard, Dreiding - a generic force-field for molecular simulations, J. Phys. Chem. 94 (26) (1990) 8897–8909.
[39] T. Liang, S.R. Phillpot, S.B. Sinnott, Erratum: parametrization of a reactive many-body potential for Mo–S systems [Phys. Rev. B79, 245110 (2009)], Phys. Rev. B 85 (19) (2012), 199903.
[40] Y. Ma, Y. Dai, M. Guo, C. Niu, B. Huang, Graphene adhesion on MoS_2 monolayer: an ab initio study, Nanoscale 3 (9) (2011) 3883–3887.
[41] Z. Li, S.Y. Xiong, C. Sievers, Y. Hu, Z.Y. Fan, N. Wei, et al., Influence of thermostatting on nonequilibrium molecular dynamics simulations of heat conduction in solids, J. Chem. Phys. 151 (23) (2019), 234105.
[42] X. Wu, V. Varshney, J. Lee, Y. Pang, A.K. Roy, T. Luo, How to characterize thermal transport capability of 2D materials fairly? – sheet thermal conductance and the choice of thickness, Chem. Phys. Lett. 669 (2017) 233–237.
[43] C. Zhi, Y. Bando, C. Tang, D. Golberg, Engineering of electronic structure of boron-nitride nanotubes by covalent functionalization, Phys. Rev. B 74 (15) (2006), 153413.
[44] N. Li, G. Lee, Y.H. Jeong, K.S. Kim, Tailoring electronic and magnetic properties of MoS_2 nanotubes, J. Phys. Chem. C 119 (11) (2015) 6405–6413.
[45] C. Kittel, in: Introduction to Solid State Physics, eighth ed., John Wiley & Sons, Inc., 2004.
[46] Z.M. Zhang, Nano/Microscale Heat Transfer, Springer International Publishing, 2020.
[47] T. Kodama, M. Ohnishi, W. Park, T. Shiga, J. Park, T. Shimada, et al., Modulation of thermal and thermoelectric transport in individual carbon nanotubes by fullerene encapsulation, Nat. Mater. 16 (9) (2017) 892–897.
[48] H.K. Dong, Z.Y. Fan, P. Qian, T. Ala-Nissila, Y.J. Su, Thermal conductivity reduction in carbon nanotube by fullerene encapsulation: a molecular dynamics study, Carbon 161 (2020) 800–808.
[49] J.M. Dickey, A. Paskin, Computer simulation of the lattice dynamics of solids, Phys. Rev. 188 (3) (1969) 1407–1418.
[50] J. Haile, I. Johnston, A.J. Mallinckrodt, S. McKay, Molecular dynamics simulation: elementary methods, Comput. Phys. 7 (6) (1993), 625-625.
[51] E. González Noya, D. Srivastava, L.A. Chernozatonskii, M. Menon, Thermal conductivity of carbon nanotube peapods, Phys. Rev. B 70 (11) (2004), 115416.
[52] C.L. Ren, W. Zhang, Z.J. Xu, Z.Y. Zhu, P. Huai, Thermal conductivity of single-walled carbon nanotubes under axial stress, J. Phys. Chem. C 114 (13) (2010) 5786–5791.
[53] P.H. Ying, J. Zhang, Z. Zhong, Mechanical properties of monolayer ternary transitional metal dichalogenides $MoS_{2x}Te_{2(1-x)}$: a molecular dynamics study, J. Appl. Phys. 126 (21) (2019), 215105.
[54] E. Debie, E. De Gussem, R.K. Dukor, W. Herrebout, L.A. Nafie, P. Bultinck, A confidence level algorithm for the determination of absolute configuration using vibrational circular dichroism or Raman optical activity, ChemPhysChem 12 (8) (2011) 1542–1549.
[55] C.L. Covington, P.L. Polavarapu, Similarity in dissymmetry factor spectra: a quantitative measure of comparison between experimental and predicted vibrational circular dichroism, J. Phys. Chem. 117 (16) (2013) 3377–3386.
[56] A.E.J. Hoffman, L. Vanduyfhuys, I. Nevjestic, J. Wieme, S.M.J. Rogge, H. Depauw, et al., Elucidating the vibrational fingerprint of the flexible metal-organic framework mil-53(al) using a combined experimental/computational approach, J. Phys. Chem. C 122 (5) (2018) 2734–2746.
[57] I.M. Felix, L.F.C. Pereira, Thermal conductivity of graphene-hbn superlattice ribbons, Sci. Rep. 8 (1) (2018) 2737.
[58] P.K. Schelling, S.R. Phillpot, P. Keblinski, Comparison of atomic-level simulation methods for computing thermal conductivity, Phys. Rev. B 65 (14) (2002), 144306.
[59] Z. Wei, F. Yang, K. Bi, J. Yang, Y. Chen, Thermal transport properties of all-sp2 three-dimensional graphene: anisotropy, size and pressure effects, Carbon 113 (2017) 212–218.
[60] P. Ying, J. Zhang, X. Zhang, Z. Zhong, Impacts of functional group substitution and pressure on the thermal conductivity of ZIF-8, J. Phys. Chem. C 124 (11) (2020) 6274–6283.